Biophysical Journal Volume 96 April 2009 2871–2887

Model Discrimination and Mechanistic Interpretation of Kinetic Data in Protein Aggregation Studies

Joseph P. Bernacki and Regina M. Murphy*

Department of Chemical and Biological Engineering, University of Wisconsin, Madison, Wisconsin

ABSTRACT Given the importance of protein aggregation in amyloid diseases and in the manufacture of protein pharmaceuticals, there has been increased interest in measuring and modeling the kinetics of protein aggregation. Several groups have analyzed aggregation data quantitatively, typically measuring aggregation kinetics by following the loss of protein monomer over time and invoking a nucleated growth mechanism. Such analysis has led to mechanistic conclusions about the size and nature of the nucleus, the aggregation pathway, and/or the physicochemical properties of aggregation-prone proteins. We have examined some of the difficulties that arise when extracting mechanistic meaning from monomer-loss kinetic data. Using literature data on the aggregation of polyglutamine, a mutant β-clam protein, and protein L, we determined parameter values for 18 different kinetic models. We developed a statistical model discrimination method to analyze protein aggregation data in light of competing mechanisms; a key feature of the method is that it penalizes overparameterization. We show that, for typical monomer-loss kinetic data, multiple models provide equivalent fits, making mechanistic determination impossible. We also define the type and quality of experimental data needed to make more definitive conclusions about the mechanism of aggregation. Specifically, we demonstrate how direct measurement of fibril size provides robust discrimination.

INTRODUCTION

Protein aggregation has been linked to a number of degenerative amyloid diseases, such as Alzheimer's, Huntington's, and the prion-related diseases. In these diseases, the mature aggregated species is typically β-sheet and fibrillar in morphology (1). Aggregation also poses problems of consequence in the manufacture of protein therapeutics: it can occur during purification, formulation, packaging, or storing of recombinant proteins and can lead to lowered yields, reduced efficacy, altered pharmacokinetic profiles, and potentially life-threatening immunological responses (2,3). The growing awareness of the importance of protein misfolding and aggregation has led to a concomitant increased interest in measuring and modeling the kinetics of protein aggregation.

In evaluating kinetic data on the aggregation of proteins and peptides, particularly with fibrillogenesis, some kind of nucleated growth mechanism has generally been invoked. Conventionally, the term ''nucleation'' has been used to indicate a localized phase transition, but the word has been appropriated to describe the onset of fibril growth. Descriptions and definitions vary, but generally, nucleated growth is considered to be characterized by 1), a sigmoidal growth curve with lag, propagation, and plateau phases; 2), a reduction in lag time with the addition of ''seeds''; and, sometimes, 3), a critical concentration below which aggregation will not occur (4–6). Sophisticated mathematical models have been developed that describe protein aggregation kinetics (e.g., (7–10)). However, application of these models for the interpretation of experimental data is challenging due to both the nature of the available experimental data and the complexity of the mathematical models. Despite these difficulties, several groups have analyzed monomer-loss kinetic data quantitatively using simplified kinetic models. It is important to note that such analysis has led to conclusions about the nature of the aggregation nucleus, the dominant pathway of aggregation, and/or the physicochemical properties of proteins that undergo aggregation.

Ferrone proposed that a simple algebraic equation describes monomer-loss kinetics adequately under some limiting conditions (11); in particular, only data at early time points (~10–20% of total monomer loss) is included. Wetzel and co-workers used this approach to analyze the aggregation of polyglutamine peptides, concluding that the aggregation nucleus is a structured monomer in equilibrium with the bulk pool of disordered monomers and that the equilibrium constant, though small, increases with increasing polyglutamine chain length (12–14). The same approach was used in studies of the aggregation kinetics of ataxin-3 (15) and β-clam proteins (16), and a similar conclusion, of an energetically unfavorable monomeric nucleus at equilibrium with the bulk unstructured monomer, was reached. Using a similar analysis, aggregation of protein L was determined to proceed via equilibrated nuclei that were dimers and/or trimers (17).

Other groups have applied a similar mechanistic scheme, but with different methods for fitting the model to the data. One method involves plotting the log of a specific time (lag time or t_{50}) versus the log of concentration, in which case the slope is equated to either $n/2$, or $(n + 1)/2$, where n is the size of the nucleus. This method was used in a study

Submitted August 7, 2008, and accepted for publication December 8, 2008.

*Correspondence: regina@engr.wisc.edu

Editor: Heinrich Roder.

0006-3495/09/04/2871/17 $2.00

doi: 10.1016/j.bpj.2008.12.3903

of yeast prion protein aggregation to conclude that Sup35p nuclei are hexamers but Sup35pNM nuclei are trimers (18).

Morris et al. argue for a different scheme: an autocatalytic mechanism, in which a slow but irreversible nucleation step is followed by further nucleation catalyzed by the reaction product (19). They derived a two-parameter analytical solution to the differential rate equations describing this mechanism, and used this model to fit kinetic rate constants to several sets of data in the literature. It is of interest that one data set came from Chen et al. (13), who had fit the data to the Ferrone approximation for nucleated polymerization. In all cases, reasonably good fits of the data to the model equation were obtained. Unlike the Ferrone approximation, data over the entire range of monomer loss was used in the model fitting; however, the fitted data were at only a single concentration. The autocatalytic model has been used by others, for example, in an analysis of insulin aggregation (20).

Somewhat more complex models have been used by a few groups. For example, a three-step mechanism that included monomer activation, nucleation, and elongation was proposed to explain FtsZ protein assembly (21). Experimental data were fit to a six-parameter model, and the resulting excellent fit was used to argue that FtsZ assembly is cooperative and proceeds via a dimeric nucleus. In another example, a fibril fragmentation step was added to a model of Sup35 aggregation (22), and the additional parameters improved model fit. In a third study, both homogeneous and heterogeneous nucleation steps, as well as fibril elongation by monomer addition, were included in the analysis of aggregation data of islet amyloid polypeptide (IAPP) (23).

In other cases, researchers have fit data to empirical equations in the absence of a specific mechanistic scheme. For example, Dubay et al. (24) collected literature data on a variety of proteins and, neglecting both the lag and plateau phases, fit the data to a simple exponential equation to extract a single rate constant; this parameter was then used to correlate to a variety of physical properties, such as hydrophobicity and charge. A similar approach was taken in an examination of the effect of mutations on acylphosphatase aggregation (25,26). Other researchers have also used exponential decay curves to fit aggregation data, and in some cases have related the exponent to a lumped kinetic parameter (27,28). The logistic and Gompertz functions have been used widely to model sigmoidal curves; examples in which these equations (or variations) were applied to protein aggregation kinetics include an examination of the effect of solution conditions on insulin aggregation (29), an investigation of aggregation of microtuble-associated protein tau (30), and studies on the effects of mutations on aggregation of glucagon (31) and IAPP (32).

In this work, we examined some of the issues that arise when fitting model equations to experimental data of protein aggregation kinetics, highlighting the difficulty in extracting mechanistic meaning from such modeling analyses. We focused primarily on fibril growth kinetics because of their importance in amyloid disease. First, we derived several kinetic models that describe competing aggregation schemes. We next created a ''test'' monomer-loss data set and fitted parameters for each of the models to the data using nonlinear regression. Since reasonable parameter values were obtained for several different models, we developed a statistical model discrimination method to compare the kinetic models. A key feature of this method is that the model rankings are weighted by the number of regressed parameters, effectively penalizing overparameterized models. We demonstrated that multiple models derived from disparate aggregation mechanisms provided equivalent fits. We conclude, therefore, that it is generally not possible to elucidate a mechanism of protein aggregation simply from analysis of monomer-loss kinetic data. We then defined the type and quality of experimental data needed to make definitive conclusions about the mechanism of aggregation. Finally, we examined the effect of ''seeding'' on monomer-loss kinetics to investigate the utility of seeding experiments in distinguishing among particular mechanisms of aggregation.

MATERIALS AND METHODS

Parameter regression

Model parameters were regressed using Athena Visual Studio 12.0 (Athena Visual Software, Naperville, IL), except where indicated. Athena Visual Studio provides a Windows-based interface for inputs into equation solving and parameter estimation programs. It employs an implicit integrator package, DDAPLUS, for solving initial-boundary value problems described by sets of mixed differential and algebraic equations (DDAPLUS is an extension of the DASSL predictor-corrector algorithm and is described in detail elsewhere (33,34)). Parameter estimation from multiresponse data is provided by nonlinear least-squares regression (sum-of-squares minimization) using the GREGPLUS algorithm described elsewhere (34,35); confidence limits on parameters are calculated from the covariance matrix. Sets of monomer-loss data at each initial concentration were considered independent responses. The modeling equations and monomer-loss kinetic data were programmed into Athena Visual Studio, along with initial guesses for the parameter values. The modeling equations were numerically integrated and the best-fit parameters and 95% confidence intervals were determined via least-squares regression.

Model discrimination

A statistically valid model discrimination procedure for multiresponse data was implemented according to the method described by Stewart et al. (36). All models were assigned equal prior probability, and the posterior probability, $P(m_j|\underline{\underline{Y}})$, of model m_j, given the monomer-loss data matrix Y, was calculated via

$$P\left(m_j|\underline{\underline{Y}}\right) \propto 2^{-p_j/2}\left|\underline{\underline{v}}_j\right|^{-v_e/2}$$
$$v_{ik} = \sum_u \left[Y_{iu} - G_{ji}(u)\right]\left[Y_{ku} - G_{jk}(u)\right], \quad (1)$$

where u is the vector of times at which the data were taken, p_j is the number of regressed parameters in model m_j, v_e is the degrees of freedom, and G_{ji} is the solution for response i of model m_j. v_e is calculated as the total number of data points (including replicates) minus the number of time points at which data were taken; if a set of monomer-loss data did not include replicates,

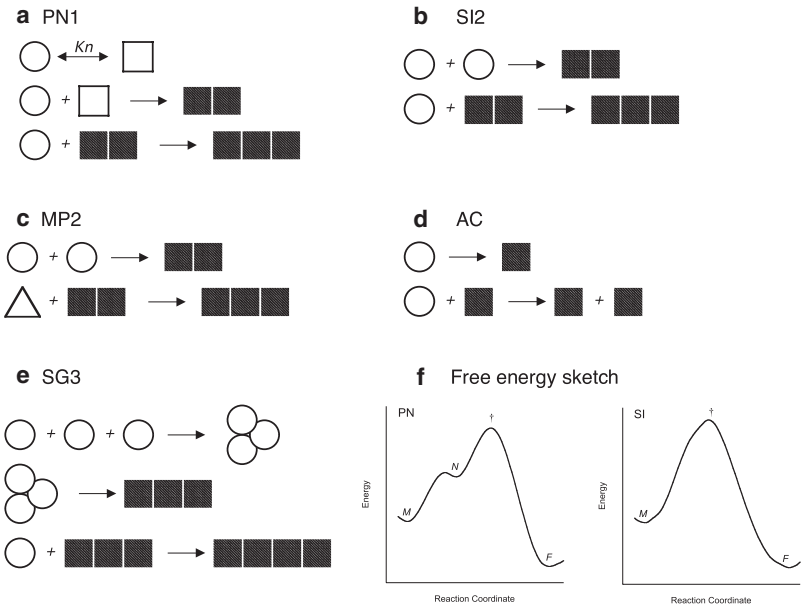

FIGURE 1 Schematics illustrating aggregation models. Open symbols indicate various conformations of monomer. Solid symbols indicate aggregates classified as fibrillar. (*a*) Preequilibrated nucleus. (*b*) Slow initiation. (*c*) Monomer partitioning. (*d*) Autocatalytic. (*e*) Sequential growth. (*f*) Qualitative Gibbs (free) energy sketches for PN and SI mechanisms. The dagger indicates a transition state. The sketch illustrates that in the PN mechanism, *N* exists as a (meta)stable species at a local energy minima; this species is absent in the SI mechanism.

v_e was set equal to 1. The matrix v_j is the covariance matrix, containing the products of the residual errors at each time point. The covariance matrix cannot have any missing values, so the data sets must be full; in other words, data must be obtained at all time points for each initial concentration. The $2^{-pj/2}$ term is obtained during the derivation of Eq. 1 (36). This term penalizes those models with a greater number of parameters, thereby offsetting the improvement in the fit of a model due to overparameterization. Thus, an increase in the number of parameters must be statistically justifiable to improve the posterior probability of the model. The posterior probabilities were normalized to give the posterior probability share π_j:

$$\pi_j = \frac{P(m_j|\underline{\underline{Y}})}{\sum_k P(m_k|\underline{\underline{Y}})}. \quad (2)$$

In essence, π_j reports on the relative likelihood that model m_j provides the best fit of the data. The numerical integration of the modeling equations and other calculations were completed using Mathematica 6.0 (Wolfram Research, Champaign, IL).

RESULTS

Mathematical models of monomer-loss kinetics

Starting with several commonly invoked mechanisms for fibril formation kinetics, we derived models describing monomer-loss and fibril-growth kinetics. We restricted our study to relatively simple models, with no more than three parameters. Qualitative descriptions or illustrations of aggregation processes will be referred to as ''schematics'', the sequence of steps describing the aggregation process will be referred to as the ''reaction pathway'', the system of differential equations derived from the reaction pathway will be referred to as the ''modeling equations'', and the numerical solution to the modeling equations will be referred to as the ''model solution''. Note that none of the reaction pathways contain true chemical reactions, in that no covalent bonds are created or broken. The schematic of each model is illustrated in Fig. 1.

Preequilibrated nucleus (PN) model

In the PN schematic, monomers (*M*) are in rapid equilibrium with a nucleus (*N*) containing *n* monomers, characterized by an equilibrium constant $K_{PN} = [N]/[M]^n$. Thus, the PN schematic posits that the nucleus exists as an identifiable species, and that the rate for interconversion between *nM* and *N* is much faster than that of subsequent steps. Typically, one assumes that $K_{PN} << 1$, because the nucleus is energetically unfavorable relative to the bulk monomer, but this is not a requirement of the mathematical formulation. Fig. 1 *f* contains a free-energy diagram that qualitatively demonstrates these concepts. Free *M* binds irreversibly to *N* to form fibril F_{n+1}, with the rate of formation described by the rate constant k_{1PN}. Fibrils grow by continued addition of *M* to F_x, where *x* indicates the number of monomers in the fibril and $x \geq n + 1$. The rate of growth is described by k_{2PN}, which is assumed to be independent of *x*. Thus, the PN reaction pathway is

$$nM \overset{K_{PN}}{\longleftrightarrow} N$$
$$M + N \xrightarrow{k_{1PN}} F_{n+1}$$
$$M + F_x \xrightarrow{k_{2PN}} F_{x+1}, x \geq n + 1$$

We set $[N] = K_{PN}[M]^n$ and $[F] = \sum_{i=n+1}^{\infty} [F_i]$, yielding the PN modeling equations

$$\begin{aligned} \frac{d[M]}{dt} &= -k^*_{1PN}[M]^{n+1} - k_{2PN}[M][F] \\ \frac{d[F]}{dt} &= k^*_{1PN}[M]^{n+1} \end{aligned}, \quad (3)$$

where $k^*_{1PN} = k_{1PN}K_{PN}$. From Eq. 3 we note that monomer-loss kinetic data cannot be used to find k_{1PN} and K_{PN}

independently. This set of coupled differential equations is solved by numerical integration given initial conditions that $[M] = [M]_0$ and $[F] = 0$ at $t = 0$. (The assumption that $[F] = 0$ at $t = 0$ is relaxed later when simulating seeding experiments.)

Ferrone approximation (FA) of the PN model

Ferrone et al. (11,13) derived a simple algebraic equation to describe the PN model monomer-loss kinetics, subject to two simplifying assumptions. First, if data are restricted to very early times, then $[M] \approx [M]_0$. Second, if monomer loss by addition to fibrils exceeds monomer loss by nucleation, then $k^*_{1PN}[M]^{n+1} << k_{2PN}[M][F]$. Application of these approximations leads to an analytic solution to Eq. 3 of

$$[M] = [M]_0 - \frac{k^*_{1PN}k_{2PN}}{2}[M]_0^{n+2}t^2 = [M]_0 - \frac{k_{1FA}}{2}[M]_0^{n+2}t^2, \tag{4}$$

where $k_{1FA} = k^*_{1PN}k_{2PN} = k_{1PN}K_{PN}k_{2PN}$. Using these approximations, the fibril growth kinetics are

$$[F] = k^*_{1PN}[M]_0^{n+2}t. \tag{5}$$

Chen et al. developed a graphical method for analyzing monomer-loss kinetic data using the FA model (13). Per Eq. 4, a plot of $[M]$ versus t^2 is linear, with slope $-0.5k_{1FA}[M]_0^{n+2}$. If data are taken at multiple initial concentrations, one can then plot the log(−slope) versus $\log[M]_0$. The slope of this log-log plot is $n+2$, and the intercept is $\log(0.5k_{1FA})$.

Slow initiation (SI) model

The SI reaction pathway consists of two irreversible steps: 1), n monomers converting to a fibril, F_n, with a rate constant k_{1SI}; and 2), M adding to F_x with a rate constant k_{2SI}.

$$nM \xrightarrow{k_{1SI}} F_n$$
$$M + F_x \xrightarrow{k_{2SI}} F_{x+1},\ x \geq n.$$

In the SI reaction pathway, the first reaction is typically considered to be slow relative to the second, but this is not a requirement of our mathematical formulation. The SI model differs from the PN model in that there is no assumption of a metastable nucleus in the former. A free-energy diagram is shown in Fig. 1 *f* that illustrates the SI model, assuming that the first reaction is slow and has a high activation energy. This first reaction step has sometimes been called nucleation by others, and the transition state (highest point on the free-energy diagram) has sometimes been called a nucleus. We do not use that terminology, instead reserving "nucleus" for the metastable species described in the PN model. Similar to the PN model, the fibril-growth rate constant k_{2SI} is assumed to be independent of fibril size and $[F] = \sum_{i=n}^{\infty}[F_i]$. The SI modeling equations are readily derived:

$$\begin{aligned}\frac{d[M]}{dt} &= -nk_{1SI}[M]^n - k_{2SI}[M][F]\\ \frac{d[F]}{dt} &= k_{1SI}[M]^n.\end{aligned} \tag{6}$$

This set of coupled differential equations was solved by numerical integration.

Autocatalytic (AC) model

In the AC reaction pathway, monomer M irreversibly converts to F_1 with a rate constant of k_{1AC}. F_1 then catalyzes the formation of additional F_1 from M with a rate constant of k_{2AC}:

$$M \xrightarrow{k_{1AC}} F_1$$
$$M + F_1 \xrightarrow{k_{2AC}} F_1 + F_1.$$

Unlike the PN and SI reaction pathways, the AC reaction pathway does not include a step for monomer loss by addition to F_x. Rather, fibrils are postulated to grow by coalescence of F_x, with $x \geq 1$. Because these modeling equations will be applied to monomer-loss kinetic data, fibril coalescence steps are not necessary in our formulation. In the AC model, one implicitly assumes that each monomer in a fibril retains its ability to catalyze further fibril formation. The modeling equations for the AC reaction pathway are

$$\begin{aligned}\frac{d[M]}{dt} &= -k_{1AC}[M] - k_{2AC}[M][F_1]\\ \frac{d[F_1]}{dt} &= k_{1AC}[M] + k_{2AC}[M][F_1]\end{aligned}. \tag{7}$$

These equations have an analytic solution:

$$[M] = [M]_0\left\{\frac{(k_{1AC} + k_{2AC}[M]_0)\exp\left[-(k_{1AC} + k_{2AC}[M]_0)t\right]}{k_{2AC}[M]_0\exp\left[-(k_{1AC} + k_{2AC}[M]_0)t\right] + k_{1AC}}\right\}. \tag{8}$$

During our analysis, we chose to numerically integrate Eq. 7. The AC model was used by Morris et al. (19) to fit a large number of sets of protein aggregation kinetic data.

Monomer partitioning (MP) model

It has been suggested that the monomer species in some systems may comprise multiple conformational states, of which only a fraction can support fibril initiation (37). To capture this schematic, the MP model posits that the monomer population partitions into two conformational subspecies, M_A and M_B, with parameter f_{MP} as the fraction of monomer in the "A" conformation. M_A and M_B are not assumed to reequilibrate with each other as fibril growth proceeds. This situation might arise, for example, upon rapid change in denaturant concentration, trapping two alternate conformations in local minimum energy wells. We assume

that the M_A subpopulation forms fibrils F_n with a rate constant k_{1MP} but does not participate in fibril growth, whereas the M_B subpopulation does not initiate new fibrils but adds to extant fibrils with a rate constant k_{2MP}:

$$nM_A \xrightarrow{k_{1MP}} F_n$$
$$M_B + F_x \xrightarrow{k_{2MP}} F_{x+1}, x \geq n.$$

Similar to previous developments, $[F] = \sum_{i=n}^{\infty} [F_i]$ and k_{2MP} is assumed to be independent of x. The MP modeling equations are

$$\begin{aligned} \frac{d[M_A]}{dt} &= -nk_{1MP}[M_A]^n \\ \frac{d[M_B]}{dt} &= -k_{2MP}[M_B][F] \qquad [M_A]_0 = f_{MP}[M]_0 \\ \frac{d[F]}{dt} &= k_{1MP}[M_A]^n. \qquad [M_B]_0 = (1 - f_{MP})[M]_0 \end{aligned} \tag{9}$$

These modeling equations have analytic solutions, for example, if $n = 1$, then

$$\begin{aligned} [M]_A &= f_{MP}[M]_0 \exp(-k_{1MP}t) \\ [M]_B &= (1 - f_{MP}) \\ [M]_0 \exp&\left[\frac{k_{2MP} f_{MP}[M]_0}{k_{1MP}}\left(1 - k_{1MP}t - e^{-k_{1MP}t}\right)\right]. \end{aligned} \tag{10}$$

We numerically integrated Eq. 9 during our analysis. To compare the modeling equations to monomer-loss data, we let $[M_A] + [M_B] = [M]$.

Sequential growth (SG) model

We considered the possibility that a soluble intermediate f forms during aggregation. In the SG model, 1), n monomers react irreversibly to form f_n with a rate constant k_{1SG}; 2), f_n converts to fibril F_n with a rate constant k_{2SG}; and 3), M adds to F_x with a rate constant k_{3SG}:

$$nM \xrightarrow{k_{1SG}} f_n$$
$$f_n \xrightarrow{k_{2SG}} F_n$$
$$M + F_x \xrightarrow{k_{3SG}} F_{x+1}, x \geq n.$$

As before, k_{3SG} is considered independent of x and $[F] = \sum_{i=n}^{\infty} [F_i]$. The SG modeling equations are

$$\begin{aligned} \frac{d[M]}{dt} &= -nk_{1SG}[M]^n - k_{3SG}[M][F] \\ \frac{d[f]}{dt} &= k_{1SG}[M]^n - k_{2SG}[f_n] \\ \frac{d[F]}{dt} &= k_{2SG}[f_n]. \end{aligned} \tag{11}$$

Soluble intermediates lack the defined structure, density, and/or morphology of fully formed fibrils and thus may not be detectable by assays such as sedimentation or thioflavin T fluorescence. We therefore assumed, in fitting the SG model to monomer-loss kinetic data, that the ''monomer'' response equals $[M] + n[f_n]$.

Simple polynomial (SP) model

For completeness, we also considered empirical polynomial models to describe monomer-loss kinetics. We limited ourselves to only linear (SP1) and quadratic (SP2) expressions:

$$[M] = [M]_0(1 - k_1 t) \tag{12}$$

$$[M] = [M]_0\left(1 - k_1 t - k_2 t^2\right). \tag{13}$$

Equations 12 and 13 do not represent any implied mechanism or reaction pathway.

It is clear that there are many variations on the above models. In particular, we neglected schemes involving mechanisms of fibril growth or restructuring other than monomer addition. We also did not consider any reaction pathways with off-path agglomeration steps, and we limited ourselves to models with no more than three parameters. One could imagine combinations of mechanisms, for example, a combination of PN and SG models where a preequilibrated nucleus is formed that then grows into a soluble aggregate before maturing to fibrils. A modular approach for combining different steps to generate a large number of combinatorial models has been described recently (38). Still, we believe this collection is sufficiently diverse for our purposes, and is reasonably representative of the kinetic models that have been published in the literature and used to interpret experimental data.

Selection of test data sets and parameter estimation

Development of representative monomer-loss kinetic data sets

Our first objective was to establish test data sets to subject to parameter estimation and model discrimination. To do this, we adapted aggregation data published by others on three different systems: the polyglutamine peptide $K_2Q_{36}K$ (13), the β-clam protein (16), and protein L (17). These data sets were chosen because they all contained kinetic data taken at several different concentrations and because all three sets were analyzed in the original literature using Eq. 4 and the log-log method described by Chen et al. (13). Our model discrimination procedure requires full response data taken at the same independent variable values (Eq. 1). Since aggregation rates generally decrease with concentration, we chose to define our independent variable not as time (t) but as $\tau = [M]_0 t$. This reflects practice, as low-concentration

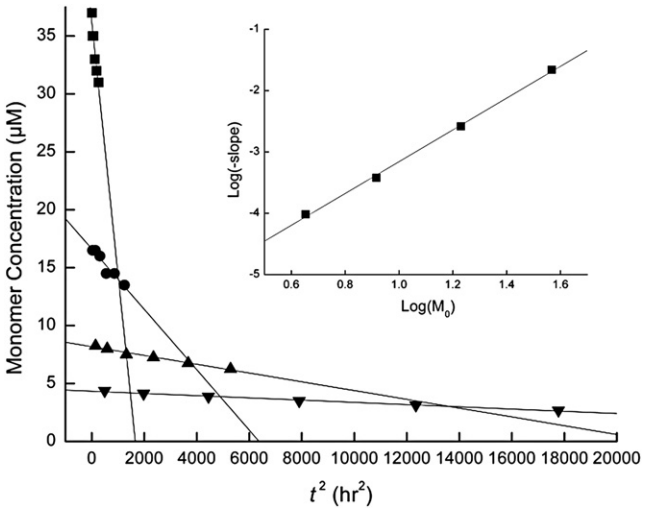

FIGURE 2 Graphical analysis of the monomer-loss kinetics of the polyQ test data, as suggested by Chen et al. (13). The initial concentrations are 37 μM (■), 17 μM (●), 8.25 μM (▲), and 4.5 μM (▼). (*Inset*) Slopes of the best-fit lines versus the corresponding initial concentration. The slope of this line is 2.59 ± 0.07, and the intercept is −5.74 ± 0.08.

samples are generally tracked over longer time periods than high-concentration samples (e.g., (13,16,17)). In no case did the published data fit the exact requirements of our model discrimination procedure. Therefore, we were not able to use the published data without modification; rather, the published data served as a template for developing test data sets. Each set will be discussed in turn.

PolyQ test data

Aggregation of polyglutamine peptide as a function of length was studied by Wetzel and co-workers as a model system for aggregation of huntingtin and related proteins that have been linked to expanded CAG domain diseases (13). Monomer-loss data for $K_2Q_{36}K_2$ were collected based on a centrifugation assay in which peptide concentration in the supernatant was measured by reverse-phase high-performance liquid chromatography. Data at four initial concentrations were reported (13). The published data did not report concentration measurements at the same τ for all initial monomer concentrations, nor were there the same number of data points for each initial concentration (three points at the two higher concentrations, and nine at the two lower concentrations). Therefore, we used the published data as a template, but we modified this template to produce a data set that was amenable to model discrimination. For example, we interpolated between the actual data points to obtain data at the τ values required. Our representative data set includes four responses (at initial concentrations of 37, 17, 8.25, and 4.5 μM) and six τ points (100, 200, 300, 400, 500, and 600 μM h) per response. These data are denoted as our ''polyQ test'' data set and are given in Table S1 in the Supporting Material.

The polyQ test data are plotted in Fig. 2 as $[M]$ versus t^2 (per Eq. 4), following the analysis procedure described elsewhere (13). The slopes for each initial concentration data set were determined by linear regression. The inset to Fig. 2 shows a plot of log(−slope) versus $\log[M]_0$. The slope of the log-log plot for the polyQ test data is 2.59 ± 0.07, similar to the reported value of 2.68 for the original published data (13). Since the slope $= n + 2$, this was interpreted in the original literature as $n \sim 1$, indicating that the nucleus is a monomer in equilibrium with the unfolded monomer pool. From the intercept of Fig. 2 (*inset*), we obtained a value of $\log(k_{1FA}/2) = -5.75 \pm 0.08$ or $k_{1FA} = 0.27$ M^{-2} s^{-2}, somewhat higher than the value of 0.09193 M^{-2} s^{-2} reported for the published data (13).

Clam test data

CRABP I (cellular retinoic acid binding protein I) is a member of the ''β-clam'' protein family whose folding kinetics have been studied in detail. A slow-folding mutant (P39A) is known to form inclusion bodies. Ignatova and Gierasch measured in vitro aggregation of this mutant using a probe that is fluorescent when bound to all nonnative states, and using centrifugation followed by concentration determination of the supernatant (16). The published data were modified slightly to meet the requirements of our model discrimination method to generate the ''clam test'' data set (Table S2). As with the polyQ test data, four concentrations at six τ points were included.

In the original literature, the data were analyzed using Eq. 4 and the method described in Chen et al. (13). It was concluded that $n \approx 1$, that aggregation proceeded via a monomeric nucleus, and that ''an unfavorable equilibrium between the misfolded intermediate and the bulk pool of monomers [was] causative in aggregation.'' We analyzed our clam-test data set using this method, to be sure that our modified data were in keeping with the original, and similarly found $n = 0.9 \pm 0.4$. (Note that only a fraction of the test data, at low-percent total aggregation, was used in this analysis, because the analysis using Eq. 4 is valid only at low aggregation. The full range of the test data set was used in subsequent parameter estimation and model-discrimination steps.)

Protein L test data

Protein L is a small α/β protein that aggregates in 25% trifluoroethanol solutions. Aggregation kinetics were measured using the thioflavin T assay (17), and the data were analyzed using Eq. 4 and the ''log-log'' method (13). From this analysis, it was concluded that the kinetic data was consistent with linear elongation with a nucleus size of 2 or 3. We adapted the published data slightly to meet the requirements of our model-discrimination procedure and generated the ''protein L test'' data set (Table S3). We analyzed this test data set using the log-log method and

TABLE 1 Fitted parameter values obtained by regression to the polyQ test data set

Model	n	r^2	k_1	k_2	k_3 or f_{MP}
PN	1	0.999	1.4 (1.1) × 10^{-4} μM^{-1} h^{-1}	5 (8) × 10^{-3} μM^{-1} h^{-1}	
	2	0.994	4 (7) × 10^{-6} μM^{-2} h^{-1}	5 (16) × 10^{-3} μM^{-1} h^{-1}	
	3	0.991	1.1 (2.5) × 10^{-7} μM^{-3} h^{-1}	5 (22) × 10^{-3} μM^{-1} h^{-1}	
FA	1	0.998	1.1 (0.1) × 10^{-6} μM^{-2} h^{-2}		
	2	0.992	3.0 (0.6) × 10^{-8} μM^{-3} h^{-2}		
	3	0.989	8 (2) × 10^{-10} μM^{-4} h^{-2}		
SN	1	0.994	1 (5) × 10^{-3} h^{-1}	2 (9) × 10^{-2} μM^{-1} h^{-1}	
	2	0.999	7 (6) × 10^{-5} μM^{-1} h^{-1}	1.1 (1.5) × 10^{-2} μM^{-1} h^{-1}	
	3	0.994	1.4 (2.4) × 10^{-6} μM^{-2} h^{-1}	1.5 (4.5) × 10^{-2} μM^{-1} h^{-1}	
AC		0.994	2.5 (2.3) × 10^{-3} h^{-1}	3.7 (2.8) × 10^{-3} μM^{-1} h^{-1}	
MP	1	0.999	1.8 (0.9) × 10^{-1} h^{-1}	5 (~) × 10^{0} μM^{-1} h^{-1}	8.8 (1.9) × 10^{-5} –
	2	0.999	7 (~) × 10^{0} μM^{-1} h^{-1}	2 (5) × 10^{0} μM^{-1} h^{-1}	5 (8) × 10^{-4} –
	3	0.998	8 (~) × 10^{3} μM^{-2} h^{-1}	6 (32) × 10^{-1} μM^{-1} h^{-1}	2 (8) × 10^{-3} –
SG	1	0.999	1.4 (0.5) × 10^{-1} h^{-1}	2.9 (1.0) × 10^{-3} h^{-1}	1.3 (0.6) × 10^{-1} μM^{-1} h^{-1}
	2	0.999	2.1 (1.4) × 10^{-4} μM^{-1} h^{-1}	1.9 (1.3) × 10^{-1} h^{-1}	1.5 (5) × 10^{-3} μM^{-1} h^{-1}
	3	0.999	5.6 (3.8) × 10^{-5} μM^{-2} h^{-1}	2.2 (0.6) × 10^{-2} h^{-1}	2 (9) × 10^{-3} μM^{-1} h^{-1}
SP1		0.991	5.1 (1.3) × 10^{-3} h^{-1}		
SP2		0.995	7.6 (1.6) × 10^{-3} h^{-1}	−5 (2) × 10^{-5} h^{-2}	

Fitted value and the 95% confidence interval (in parentheses) are shown for each parameter. A tilde (~) in place of a numerical confidence interval indicates an indeterminate parameter.

found $n = 2.6 \pm 0.5$, again demonstrating that our data set is consistent with the published data.

Parameter estimation

The three test data sets were then used to obtain parameter values by fitting each of the kinetic models to each data set using the parameter estimation package Athena Visual Studio. Where applicable, n was fixed to an integer value of 1, 2, or 3; these models are denoted as, e.g., PN2 for the preequilibrated nucleus model with $n = 2$. In total, 18 different models were fitted to three different test data sets. All modeling equations were modified to accommodate the transformation of the independent variable from t to τ.

A summary of the fitted parameters for the polyQ test data is given in Table 1. We were able to determine numerical values for all parameters, though in many cases the confidence interval was very large. Confidence intervals were generally smaller for those models with fewer parameters. There are several specific results worth noting.

1. The fitted value of k_{1FA} was 0.084 ± 0.01 M^{-2} s^{-2}, roughly a factor of 3 smaller than the value obtained from fitting Eq. 4 using the log-log method. This discrepancy can be attributed primarily to the difference between setting $n = 1$ and fitting to $n = 0.59$.
2. If the Ferrone approximation is adequate to analyze the polyQ test data, then we should observe $k_{1FA} = k^*_{1PN}k_{2PN}$. A comparison of the fitted values in Table 1 reveals that k_{1FA} is ~35–45% larger than $k^*_{1PN}k_{2PN}$, depending on the chosen value of n. This difference represents the error imposed by the two simplifying assumptions used to derive Eq. 4.
3. With the SI model, the first reaction is indeed slower than the second reaction. This is most directly observed at $n = 2$; at $n = 1$ or $n = 3$ the comparison requires consideration of the monomer concentration.
4. For the MP model, the fraction of monomer capable of initiating fibril formation is strikingly small. However, the uncertainty in the parameter values is large, due to the high correlation between f_{MP} and the rate constants.
5. In the SG model, formation of the soluble intermediate f is faster than conversion of f to F; thus, f accumulates during early times.

The r^2 values for each fit are listed in Table 1; no r^2 value was <0.989, which is usually taken to indicate a good fit for each model. Visual confirmation of the adequacy of the fit was obtained by plotting the fitted curves against the test

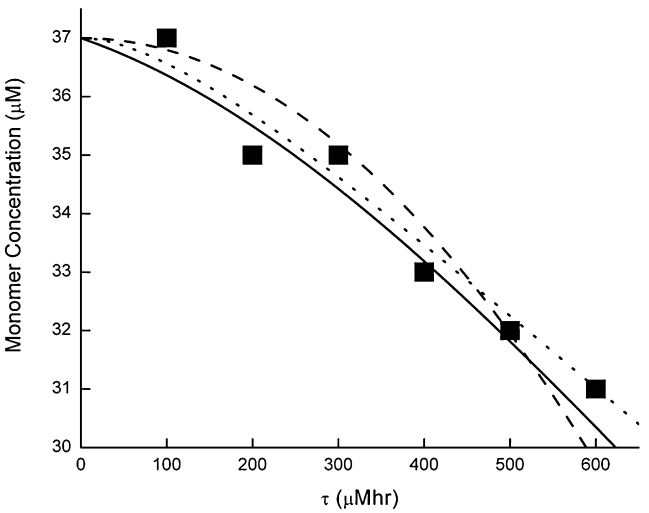

FIGURE 3 Representative model solutions for the polyQ test data set. The 37 μM test data (■) and the corresponding PN1 (*solid line*), FA1 (*dashed line*), SI2 (*dash-dotted line*), and SG3 (*dotted line*) model solutions are plotted against the transformed time variable as $\tau = [M_0]t$. The SI2 and PN1 model solutions for 37 μM are virtually indistinguishable at this resolution.

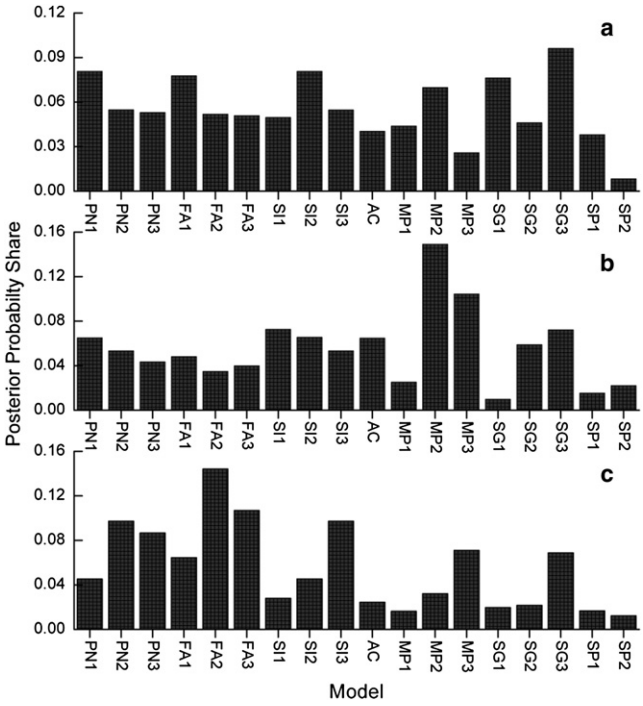

FIGURE 4 Model discrimination results for the (*a*) polyQ test, (*b*) clam test, and (*c*) protein L test data sets. (*a*) For the polyQ test data, the SG3 model has the highest share (0.096), followed by the SI2 (0.081), PN1 (0.081), FA1 (0.078), SG1 (0.076), and MP2 (0.070) models. (*b*) For the clam test data, the MP2 has the highest share (0.15), followed by the MP3 (0.10), SI1 (0.073), and SG3 (0.072) models. (*c*) For the protein L data, the FA2 has the highest share (0.14), followed by the FA3 (0.11), SI3 (0.097), and PN2 (0.097) models.

data; a selection of model solutions is plotted against the 37 μM Poly Q test data in Fig. 3.

Similarly, the clam test and protein L test data sets were fit to the 18 various kinetic models. In all cases, parameter estimates were obtained by nonlinear regression, and good fits, as characterized by r^2, were observed (not shown).

Model discrimination of three test data sets

We next applied our model discrimination procedure to evaluate the competing kinetic models. The modeling equations were numerically integrated using the fitted parameter values (shown for polyQ (Table 1), but not for clam and protein L test sets) to obtain the model solutions versus τ. Equations 1 and 2 were used to calculate the normalized posterior probability of each model on the basis of the test data set. We will discuss each test data set in turn.

Results of our evaluation of the validity of various models to describe the polyQ test data are plotted in Fig. 4 *a*. None of the kinetic models is a clear winner. The SG3 model has the greatest posterior probability share, though the PN1, FA1, SI2, MP2, and SG1 models also have sizable shares. Furthermore, many of the other models do not lag far behind; most notably, the PN and FA models with $n = 2$ or 3 possess ~65% of the posterior probability share of the PN1 and FA1 models. We conclude that the correct mechanism cannot be reliably ascertained from the data (Fig. 2 and Table S1), as there is no single model with a dominating posterior probability share. Specifically, this analysis shows that these data are insufficient to draw the conclusion that polyglutamine aggregation proceeds via a preequilibrated-nucleation mechanism with a monomeric nucleus.

We completed a similar analysis of the clam test data to calculate the posterior probability of each model. For this case, the MP2 model was deemed the most probable (Fig. 4 *b*). PN1, the model chosen in the literature, was less than half as likely as MP2 to be the appropriate model. Furthermore, several other models had posterior probabilities similar to PN1, indicating that they are equally adept at describing the experimental data. Thus, one cannot conclude based on this monomer-loss data that β-clam protein aggregation proceeds through a misfolded intermediate that serves as a monomeric nucleus. Our analysis suggests that the most probable mechanism involves the presence of two alternate protein conformations at initiation of aggregation, only one of which is capable of initiating aggregation. However, conclusive evidence for this is lacking, as several other kinetic models had nonnegligible probabilities.

For the protein L test data, there was again no clearly superior kinetic model. The FA2 model yielded the highest probability (Fig. 4 *c*). It is interesting that the PN2 model, from which the FA2 is obtained via simplifying assumptions, achieves less probability share than FA2. This could be due to the narrow timescale and concentration range over which the original data were collected; there is no added benefit of the PN2 model over FA2 at fitting long-time data, and PN2 is penalized because of its additional parameter. A variety of other models (PN3, FA3, SI3, MP3, and SG3) have similar posterior probabilities. Our analysis supports a conclusion that the reaction is second- or third-order, but no definitive distinction among the various mechanisms can be made, and one cannot conclude definitively that aggregation proceeds via a dimeric or trimeric preequilibrated nucleus.

In summary, with three different sets of monomer-loss kinetic data derived from the literature, we were able to obtain good fits of the data to several kinetic models. We developed a method to discriminate among different models and determine which was the most probable. We demonstrated that although some models could be ruled out in each case, the data sets were insufficient to positively determine a unique mechanism of aggregation.

Effect of experimental error and data quantity

We next asked, given ''data'' generated from a model solution, 1), will our parameter estimation method recover the correct parameter values? and 2), will our model discrimination procedure successfully identify the correct model and eliminate incorrect models?

TABLE 2 Fitted parameters for the PN1 model regressed to simulated data sets

Data set	k^*_{1PN} (10^{-4} μM^{-1} h^{-1})	k_{2PN} (10^{-4} μM^{-1} h^{-1})
Input parameters	1.4	54
Simulation 1	0.11 (~)	1300 (200)
Simulation 2	0.0025 (~)	58,000 (8000)
Simulation 3	0.8 (1.7)	100 (300)
Triplicate	1.6 (1.1)	40 (60)
Extensive	1.1 (0.5)	77 (48)
Fibril	1.4 (0.2)	52 (16)
Time	1.0 (0.9)	73 (71)
Fibril + time	1.4 (0.1)	54 (5)

Data sets were obtained by solving the PN1 model equations at the input parameter values and then adding a random error to the calculated values. The data were then regressed to the model equations. Ideally, the input parameters would be returned. The values presented are the fitted parameters (95% confidence interval).

To explore these questions, we chose the PN1 model and the fitted parameters from the polyQ-test data set: $k^*_{1PN} = 1.4 \times 10^{-4}$ μM^{-1} h^{-1} and $k_{2PN} = 5.4 \times 10^{-3}$ μM^{-1} h^{-1}. We chose four initial concentrations ($[M]_0 = 40$, 30, 20, or 10 μM) and six transformed time points ($\tau = 100$, 200, 300, 400, 500, and 600 μM h). Equation 3 was numerically integrated with $n = 1$ to calculate $[M]$ versus τ. A normally distributed random number with $\sigma = 1$ μM was added to the calculated values to simulate experimental error. This process was repeated three times to generate three sets of simulated monomer-loss data; these data sets will be referred to as simulation 1, simulation 2, and simulation 3. These simulated data sets are available in Table S1.

The three simulation data sets were first analyzed using Eq. 4 and the graphical method described earlier (13). The n values determined in this manner were 1.7 ± 0.2, 0.4 ± 0.3, and 0.8 ± 0.3. This simple examination shows that analysis of monomer-loss data using Eq. 4 could lead to erroneous conclusions about the nucleus size, even presuming that the PN mechanism is correct, because of the influence of experimental error. The values of k_{1FA} obtained in this manner for each data set were, respectively, 0.0082, 0.59, and 0.13 M^{-2} s^{-2}; given that $k_{1FA} = k^*_{1PN}k_{2PN}$, the anticipated value was 0.058 M^{-2} s^{-2}. Again, we observe that experimental error can lead to large variability in parameter estimates when this methodology is used.

We next evaluated the simulated data using our parameter-estimation and model-discrimination procedures, to determine if we could 1), recover the input model parameter values; and 2), uniquely ascribe the data source as the PN1 model solution. Fitted PN1 parameter values are provided in Table 2. The regressed parameter values differed from each other by one or more orders of magnitude. This result was surprising, given that all three data sets were acquired by simply incorporating error (2.5–10% relative error, depending on the initial concentration) into the exact model solutions. Note, however, that the product of the two parameters ($k^*_{1PN1}k_{1PN1} = 0.11$, 0.11, and 0.062 M^{-2} s^{-2}) does not vary nearly as much as the individual values, nor is there as much variability as when the data were fit to Eq. 4 using the graphical method. This indicates that the lumped parameter can be ascertained with better certainty than the individual parameters, and that the two parameter values are highly correlated with each other.

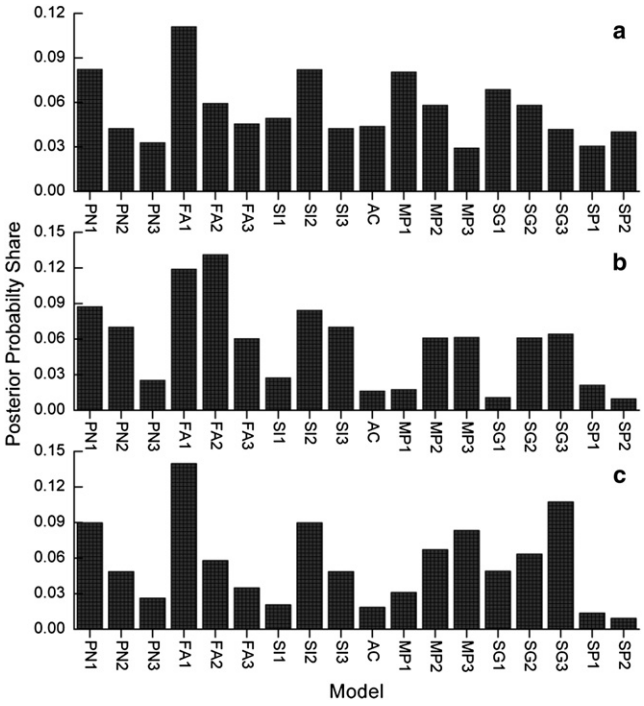

FIGURE 5 Model discrimination results for the data sets from (*a*) simulation 1 (*b*) simulation 2, and (*c*) simulation 3. The models with the highest posterior probabilities are the FA1 (0.11) for simulation 1, FA2 (0.13) for simulation 2, and FA1 (0.14) for simulation 3.

Finally, the simulation data sets were fit to all 18 kinetic models to find model parameters. The normalized posterior probabilities obtained from evaluating model fits to the simulated data are shown in Fig. 5. It was surprising that the PN1 model, from which the data were actually derived, was never the highest-ranking model. Rather, the FA model was selected for all three data sets as most probable. The FA1 model had the highest posterior probability for simulation 1, and the FA2 was the highest for simulation 2, even though the graphical method indicated the reverse: a dimeric nucleus for simulation 1 and a monomeric nucleus for simulation 2. In no case was the FA model strongly preferred over all other models, and the next-best models varied significantly among the different simulation data sets. We suspect that the FA models do relatively well for two reasons: first, they incur the smallest parameterization penalty (Eq. 1), and second, there is insufficient data at long times to provide an advantage to the PN model that compensates for the additional parameter.

We wondered whether an increase in the quantity of data would improve parameter estimation and/or model discrimination. Specifically, we evaluated the importance of replicate

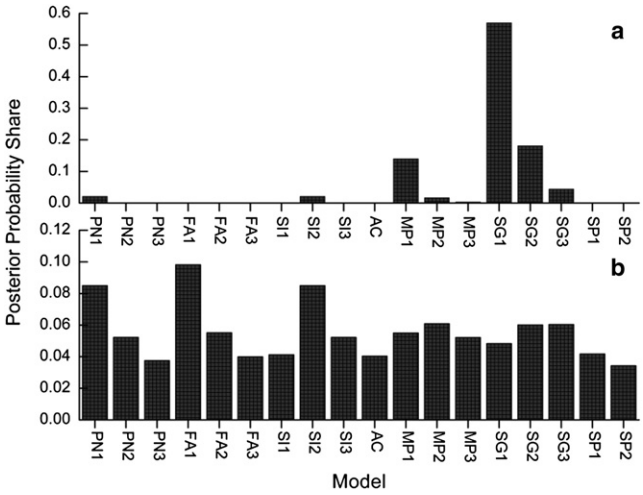

FIGURE 6 Model discrimination results for the (*a*) triplicate and (*b*) extensive data sets. The SG1 model has the largest share for the triplicate data set (0.57), whereas the FA1 model has the largest share for the extensive data set (0.098).

measurements at each time point and the addition of more data points. We generated two new simulated data sets from the PN1 model. The ''triplicate'' simulated data set had three ''measurements'' for each initial concentration (40, 30, 20, and 10 μM) at each τ value (100, 200, 300, 400, 500, and 600 μM h), whereas the ''extensive'' simulated data set had 100 single ''measurements'' taken much more frequently over the same τ range (6, 12, 18 … 588, 594, 600 μM h). The triplicate and extensive data sets are given in Table S1 and Table S4, respectively.

Graphical analysis of the triplicate data set produced an estimate of $n = 1.0 \pm 0.1$, consistent with the PN1 model used to simulate these data. Furthermore, fitted parameter values for the PN1 model were close to the input values, although the confidence intervals were still large (Table 2). Thus, replicate measurements greatly improve the reliability of parameter estimates. However, the model discrimination results did not improve (Fig. 6 *a*); indeed, the SG1 model had the highest posterior probability share by a considerable margin. With the large number of replicates in the triplicate data set, v_e is large, and a slight decrease in the residual error confers a significant advantage (Eq. 1); as such, the influence of the parameterization penalty lessens as the number of replicates grows. This may explain why a three-parameter model such as the SG1 is selected over the two-parameter PN1 model. Thus, including replicate measurements greatly improves the accuracy of parameter estimates once a mechanism is assumed. Replicates become increasingly important as the number of parameters and the model complexity increase. However, replicates alone are not sufficient to successfully discriminate among alternative mechanisms.

In the extensive data set, we increased the number of data points (without replicates) within the same transformed time domain. Graphical analysis of this data set based on Eq. 4 yielded a value of $n = 0.76 \pm 0.01$. Regression to the PN1 model led to parameter estimates that are close to the input values, with tighter confidence intervals than those obtained with the triplicate data set (Table 2). FA1, PN1, and SI2 were selected as the most probable models (Fig. 6 *b*), with several other models having smaller, but still significant, probability shares. Thus, a unique mechanism cannot be identified from these data with any confidence. We conclude that increasing the quantity of experimental data improves parameter estimation but not model identification.

Data requirements for successful model discrimination

Our analysis showed that replicates or an increased number of data points improve parameter estimation but not model discrimination. We next explored whether changing the nature of the experimental data would improve model discrimination. We examined two cases: 1), fibril-growth kinetics in addition to monomer-loss kinetics; and 2), monomer-loss data collected over much longer timescales.

Addition of fibril-growth data

The PN, FA, SI, MP, and SG models all include equations for fibril growth. Note that [*F*] in Eqs. 3, 5, 6, 9, and 11 is the molar concentration of fibrils, not the mass concentration. It is possible to calculate the molar fibril concentration from simultaneous measurement of the mass of fibrils and the average fibril molecular weight, obtained directly or indirectly through static light scattering, atomic force microscopy, or other experimental techniques. Because these measurements are more difficult to carry out, there is much less published data on fibril size and growth kinetics than on monomer-loss kinetics. With the AC model, fibril size is irrelevant as the fibrils are presumed to grow by an unspecified coalescence mechanism. The SP model is an empirical fit of monomer-loss data and therefore does not provide a means for calculating [*F*] versus time. Therefore, we did not include the AC or SP models in this analysis.

We again used the PN1 model with $k^*_{1PN} = 1.4 \times 10^{-4}$ μM^{-1} h^{-1} and $k_{2PN} = 5.4 \times 10^{-3}$ μM^{-1} h^{-1} to generate the simulated data. We obtained model solutions at four different initial concentrations (40, 30, 20, and 10 μM) through numerical integration of Eq. 3 and calculated [*F*] as well as [*M*] versus τ. Random normally-distributed errors ($\sigma_M = 1$ μM , $\sigma_F = 0.07$ μM) were added to simulate experimental error; the variance for the simulated fibril data was chosen to give the fibril data a similar percent error as the monomer data. This ''fibril'' data set spans the same τ range (0–600 μM h), but contains 10 rather than six data points at each concentration, to maintain the matrix dimensions necessary for model discrimination (Eq. 1). The fibril data set is provided in Table S5.

We first fit the PN1 model equations to the fibril data set to obtain estimates of the model parameters. Inclusion of fibril

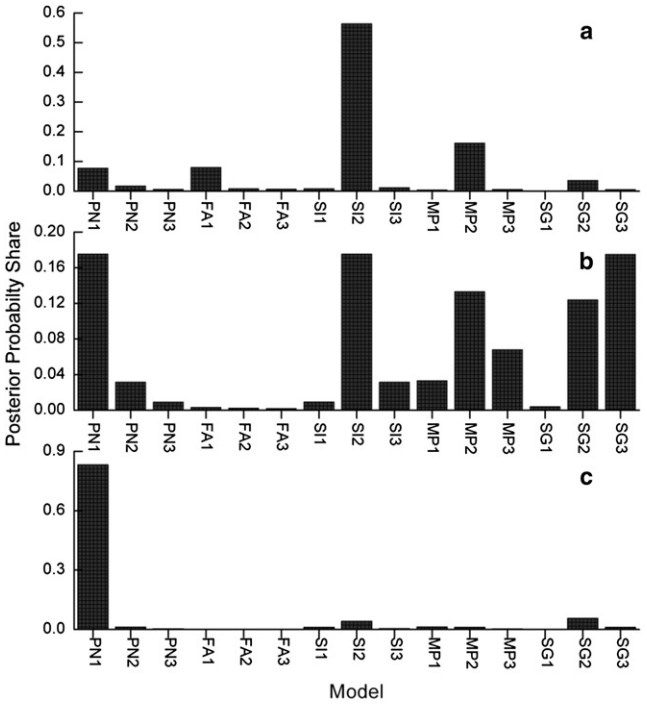

FIGURE 7 Model discrimination results for the (*a*) fibril, (*b*) time, and (*c*) fibril + time data sets. The SI2 has the largest share (0.56) for the fibril data set, three models tie for the largest share (0.18) for the time dataset, and the PN1 has the largest share (0.83) for the fibril + time dataset.

kinetic data greatly improved the accuracy and precision of the parameter estimates (Table 2). We next fit the fibril data set to the PN, FA, SI, MP, and SG models at $n = 1$, 2, and 3, and calculated the normalized posterior probability. It was surprising that the SI2 model had a much greater posterior probability share than the PN1 model from which the data were actually obtained (Fig. 7 *a*). This is akin to a false positive; analysis of this data set would lead to the conclusion that the slow-initiation model with $n = 2$ was superior to the model actually used to generate the simulated data.

Increased percent monomer loss

We next tested whether including data over a longer time period, and thus a greater percent monomer loss, would improve parameter estimation and model discrimination. We simulated monomer-loss data directly versus t, rather than versus the scaled time variable, τ. The time range was chosen so that ~90% of the monomer at $[M]_0 = 40$ μM aggregated over the course of the ''experiment''; the six time points used were 15, 30, 45, 60, 75, and 90 h. The time data set is included in Table S5. The parameter regression was improved in comparison to the simulation data sets (Table 2). Collecting data over a longer time period also somewhat improved model discrimination, in that more models were determined to be unsatisfactory (Fig. 7 *b*). The FA models were clearly unable to describe this data set, which is to be expected, as the approximations leading

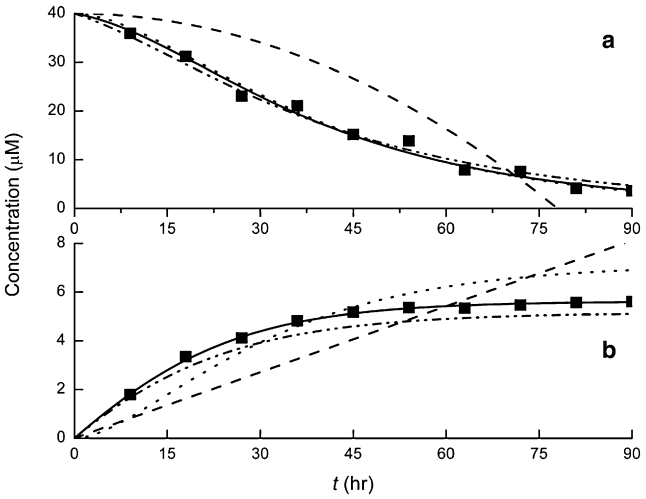

FIGURE 8 Representative model solutions for the fibril + time data set. The 40 μM monomer-loss (*a*) and fibril-growth (*b*) data (■) and the corresponding PN1 (*solid line*), FA1 (*dashed line*), SI2 (*dash-dotted line*), and SG3 (*dotted line*) model solutions are plotted versus time.

to the FA equations are reliable only when there is little (~10–20%) monomer loss. Still, there were several models with similar probabilities; these included the correct model (PN1) as well as various incorrect models (SI2, MP2, SG2, and SG3).

Addition of fibril data plus increased percent monomer loss

Finally, we combined both ideas: the ''fibril + time'' data set (Table S5) included fibril data and was measured versus t to ~90% monomer loss. At each initial monomer concentration, data was generated at 10 equally spaced time points up to 90 h. Both parameter estimation and model discrimination were highly successful with the fibril + time data set. Parameter estimates obtained by fitting to the PN1 model equations were identical to the input values, and the confidence intervals were small (Table 2). Furthermore, the PN1 model was selected as the correct model via our model-discrimination analysis: the posterior probability of the PN1 model was more than an order of magnitude higher than the next best model (Fig. 7 *c*). A comparison of the data and model solutions at $[M]_0 = 40$ μM is given in Fig. 8. Though many of the competing models successfully track the monomer-loss data (Fig. 8 *a*), only the source PN1 model also captures the fibril data without systematic deviation (Fig. 8 *b*). Most notably, the model discrimination analysis of the fibril + time data successfully indicated the correct model despite excellent fits from the competing models. Ten of the 12 models had r^2 values >0.95, with the SG2 model nearly matching the r^2 of the source PN1 model (0.989 vs. 0.990). Thus, a high r^2 value alone is not sufficient to conclusively identify a particular kinetic scheme as correct.

To ensure that our conclusions are general, and not specific to PN-type aggregation mechanisms, we expanded

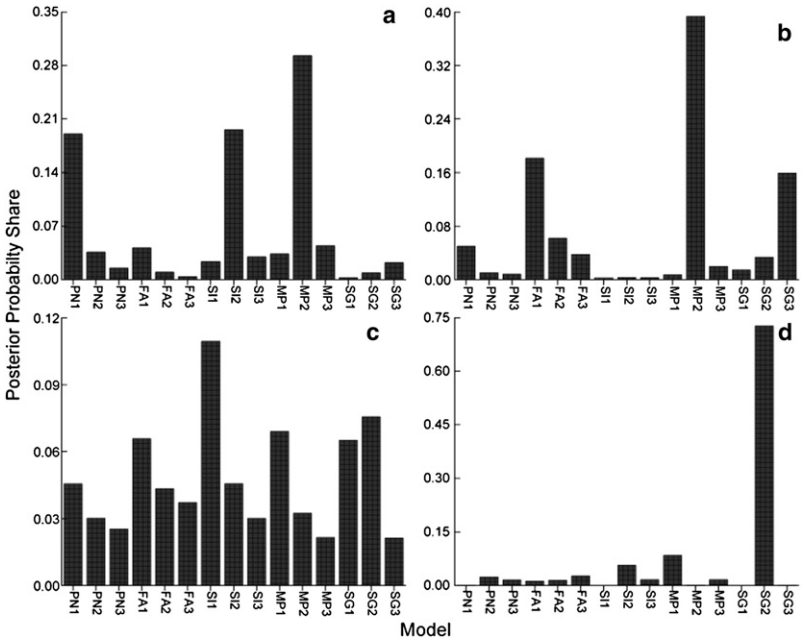

FIGURE 9 Model discrimination results for the (*a*) MP2 simulation, (*b*) MP2 fibril + time, (*c*) SG2 simulation, and (*d*) SG2 fibril + time data sets.

our analysis to include two other mechanisms, MP2 and SG2. Model equations were solved, using parameters obtained by fitting the clam (MP2) or protein L (SG2) test data sets. These solutions were then used to generate either monomer-loss data (''MP2 simulation'' or ''SG2 simulation''), or monomer-loss plus fibril-growth data to ~90% total aggregation (''MP2 fibril + time'' or ''SG2 fibril + time''). Experimental error was added to each solution generated by the models, and then the resulting simulated data sets were fitted to the various kinetic models. The data sets used in this analysis are given in Table S2, Table S3, Table S6, and Table S7.

Results of this analysis are summarized in Fig. 9. With the MP2 simulation data, our model discrimination process was able to identify the MP2 model as the most probable (Fig. 9 *a*), but two other models, the SI2 and the PN1, also had substantial posterior probabilities. Addition of the fibril-growth data increased the MP2 probability and provided for more robust identification of the correct mechanism (Fig. 9 *b*).

Model discrimination was poor with the SG2 simulation data (Fig. 9 *c*) as was found with the PN1 simulation (Fig. 5). Marked improvement was obtained if fibril-growth data was analyzed along with monomer-loss data, and the data were collected over most of the aggregation process (Fig. 9 *d*). In this case, SG2 was clearly identified as the correct model.

Thus, we conclude that both monomer-loss and fibril-growth data, extending over nearly the entire aggregation process, are necessary to discriminate between competing aggregation models. It is important to point out that the complementary statement can also be made: given monomer-loss and fibril-growth data extending over the aggregation process, discrimination among different aggregation mechanisms is robust, and the correct model can be identified.

Characteristics of nucleated growth: concentration-dependent lag times and seeding

A lag time that decreases with concentration and the elimination of this lag phase by the addition of preexisting fibrils (''seeding'') are frequently considered to be diagnostic of nucleated growth (4,6,8,16,28,39,40). We examined which of our models were able to capture these behaviors.

To do this, we used the parameter estimates in Table 1, then obtained model solutions at $[M]_0 = 0.1\ \mu$M, 0.5 μM, and 1.0 μM. Depending on the concentration and parameter values, all models were able to produce sigmoidal monomer-loss profiles, with apparent lag phases (not shown). We note,

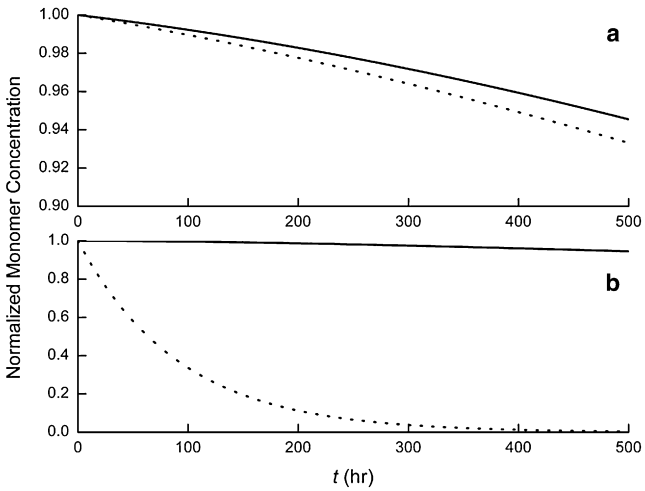

FIGURE 10 Effect of seeding. The initial concentrations simulated were $[M]_0 = 0.5\ \mu$M and $[F]_0 = 0\ \mu$M (*solid lines*) and $[M]_0 = 0.5\ \mu$M and $[F]_0 = 0.005\ \mu$M (*dotted lines*). Solutions for the PN1 (*a*) and MP2 (*b*) models were obtained using the parameter values listed in Table 1.

however, that none of the models produced true lag phases, if we define a true lag phase as a time period during which there is no aggregation. A true lag phase requires a stochastic aggregation model. Rather, the apparent lag phase we observed is indicative of a slow aggregation rate during early times and a faster aggregation rate at intermediate times. With the exception of the AC and SG1 models, the lag time decreased strongly with concentration. For example, with the MP2 model, the time to 1% aggregation increased from 86 h at $[M]_0 = 1.0\ \mu$M to 864 h when $[M]_0 = 0.1\ \mu$M. We conclude that sigmoidal monomer-loss kinetics and a concentration-dependent lag time are not diagnostic of any unique aggregation model.

We simulated seeding by using a nonzero $[F]$ at $t = 0$. Specifically, we calculated the monomer-loss profiles with $[M]_0 = 0.5\ \mu$M and $[F]_0 = 0.005\ \mu$M, using the parameter values given in Table 1. We were surprised to find that there was virtually no change in monomer-loss kinetics with the PN1 model (Fig. 10 *a*), whereas a drastic seeding effect was observed with the MP2 model (Fig. 10 *b*). There was no effect of seeding in the AC or SG1 models, small effects with PN2, SI1, SI2, SG2, and SG3, and moderate effects with PN3 and SI3; the largest effect of seeding was observed with the MP series of models (not shown). Thus, we conclude that the absence of a significant seeding effect does not necessarily rule out nucleated growth, nor does the presence of a seeding effect provide definitive proof of any specific aggregation mechanism. Furthermore, seeding experiments cannot be used in model discrimination unless the molar fibril concentration is known; in most published experiments, only the fibril mass concentration is reported.

DISCUSSION

Protein aggregation, and particularly fibril growth, has received considerable attention over the past few years because of its negative effects in degenerative amyloid diseases and in the manufacture of protein pharmaceuticals. On a more positive front, controlled self-assembly of peptides and proteins into supramolecular structures affords the opportunity to design novel materials with unique functional properties. Knowledge of the pathway by which aggregates form, and their rate of formation, is critical information as researchers aim to develop methods and reagents for reliable control of aggregation.

There is a growing body of literature in which the kinetics of protein aggregation is measured quantitatively and the data are interpreted mechanistically. A simple, but widely used, approach for quantitative analysis of kinetic data is illustrated in other studies (13,15–17). By limiting data analysis to the first ~10–20% of the aggregation process and by assuming that the rate of fibril elongation exceeds that of fibril nucleation, a simple algebraic expression (Eq. 4) is derived. Monomer concentration is predicted to decrease with a t^2 dependence, and monomer-loss kinetics are characterized by a single lumped rate constant, k_{1FA}, and the size of the aggregation nucleus, n. This algebraic equation, first described by Ferrone (11), is derived from a more complete nucleation-based aggregation model; this model assumes that monomers are in rapid and reversible equilibrium with an energetically unfavorable nucleus, and that this nucleus (and subsequent fibrils) grows by monomer addition. It is important to note that the conclusions derived from this type of analysis have been used to motivate and inform theoretical studies on the structure of the nucleus (e.g., (41)) and the connection between aggregation and toxicity (e.g., (28)). However, there has not been a systematic evaluation of the validity of applying Eq. 4 to kinetic data or the robustness of any mechanistic interpretation based on the outcome of this analysis.

Some researchers have applied more detailed and sophisticated kinetic models to analyze their data. For example, Collins et al. derived differential equations for aggregation of the yeast prion protein Sup35 that included nucleation, growth, and fibril fragmentation steps, but they fit only a linearized version of the model to their data (22). Ruschak and Mirankar (23) derived a set of differential equations involving three rate constants for primary nucleation, secondary nucleation, and elongation. All steps were assumed irreversible and the rate constants were fit to kinetic data for IAPP aggregation. Assembly of the FtsZ protein, as measured by a fluorescence assay, was fit to a six-parameter model that included forward and reverse steps for monomer activation, dimerization, and elongation (21). The researchers reported that they achieved an excellent fit to the model. In a very recent report, Xue et al. (38) developed a clever modular approach for generating a library of aggregation models. Kinetic data on β_2-microglobulin aggregation were collected to obtain lag times and lumped rate constants. Several models were fitted to these parameters by least-squares regression, and the models were ranked based on goodness-of-fit criteria, with a penalty assessed based on the number of parameters. The spirit of this work is similar to ours, although the approaches and goals are distinct.

The goals of this work were 1), to examine the validity of Eq. 4 in fitting experimental kinetic data; 2), to compare the accuracy of parameter estimates obtained from linearized, graphical approaches versus nonlinear regression methods; 3), to develop a method for discriminating among different kinetic formulations; and 4), to define the nature of the experimental data needed for robust parameter estimation and model discrimination.

Experimental issues

Experimental methods for measuring fibril formation kinetics include thioflavin T fluorescence, turbidity, sedimentation, size exclusion chromatography, circular dichroism, and filtration assays. In general, these techniques report (or are assumed to report) the mass of protein/peptide in the fibrillar state or the mass of nonaggregated monomer, which are often

presumed to be equivalent. Some difficulties arise in interpreting the data obtained using these methods. For example, small soluble oligomers will not be differentiated from monomers in filtration or sedimentation assays, and such oligomers will not be detected by circular dichroism if they lack regular secondary structure. Thioflavin T fluorescence is insensitive to nonamyloid aggregation, and because the dye binds to the surface of large aggregates and its fluorescence intensity is partially dependent on morphology, the technique might not accurately assay the mass of fibrils. To maintain our focus on data fitting and model discrimination, we did not consider these experimental uncertainties in our analysis. Following along with the general practice, we assumed that measurements of monomer concentration were reliable and, except where otherwise noted, that only monomers and fibrils were present.

Parameter estimation

Equation 4 is derived from the PN mechanism, but data analysis using Eq. 4 requires the application of two simplifying assumptions. The graphical method recommended by Chen et al. (13) requires further transformations of the data that can skew the experimental errors so that they are no longer randomly distributed. We evaluated the ''polyQ test'' data set and found, when the data were analyzed, that there was as much as a fourfold difference in the lumped rate constant k_{1FA} obtained using 1), the graphical log-log method; 2), nonlinear regression fit directly to Eq. 4; or 3), nonlinear regression via numerical integration of the PN model equations (Eq. 3). We also found that the log-log method was sensitive to experimental error; for example, within our three simulation data sets, estimates of n varied from 0.5 to 1.7, and the lumped rate constant varied from 0.0082 to 0.59 M^{-2} s^{-2}. Thus, extreme care must be taken not to place too much confidence in the numerical values of n or k_{1FA} obtained by these methods.

We next evaluated the ability of a nonlinear regression multiresponse analysis method to fit kinetic data to a variety of model equations. Our three test data sets were developed from published data from three different sources (13,16,17) and are representative of the type of data that is generally available for kinetic analysis. It was interesting that we were able to obtain fitted parameter values for almost all of the models that we attempted. Confidence intervals varied significantly; as a general rule, fewer fitted parameters meant tighter confidence intervals. For example, in fitting the polyQ test data set to the PN1 model, we obtained parameter estimates with large confidence intervals, whereas the same data set fit to the FA1 model generated a lumped parameter with a small confidence interval (Table 1). This result is initially surprising, as FA1 represents an approximate solution to the full PN1 model, but it is most likely because of high correlation between the two PN1 parameters; in other words, the product of the PN1 parameters is known more accurately than the individual parameter values. This analysis suggests that parameter error estimates from overly simplified models may be misleadingly small. On the other hand, although more complex models (which include for instance fibril fragmentation or secondary nucleation) may more accurately describe the true physical situation, the increased number of unknown variables increases the uncertainty of fitted parameter values.

The quantity and nature of the experimental data also greatly affects the quality of the resultant parameter estimates. We show (Table 2) that replicate experiments, more frequent data collection, and expansion of the time over which monomer-loss data are taken all improve the reliability of the parameter estimates. These factors must be carefully considered in the experimental design.

However, a good fit of a model to data does not mean that the underlying mechanism must be correct! When we simulated data using one model, and then fit alternate models to the simulated data, we were able to obtain parameter estimates for nearly all of the models (data not shown). As such, we disagree with the statement that obtaining a good fit indicates that the ''mechanism must be portraying at least some of the key features of the more complete, elementary step process of protein agglomeration'' (19). We frequently obtained ''good'' parameter estimates (i.e., small confidence intervals) and ''good'' fits (i.e., high r^2) with models that did not earn a high posterior probability. Thus, one must not interpret a good fit as equivalent to identification of the correct mechanism.

Model discrimination

Parameter estimation is only the first step in identifying the aggregation mechanism from data. The next step is determination of the uniqueness of the proposed mechanism at fitting the experimental data. The model discrimination method we demonstrate here evaluates the probability that a specific model is the best model, given a library of alternatives. Of importance, we penalize models that require additional parameters; a better fit should nearly always be obtained by adding parameters, but the addition of parameters must be justified by providing a statistically superior fit of the data. In other words, the added complexity of the model must be required by the data.

Our results clearly show that it is essentially impossible to select a unique mechanism among candidate models based solely on monomer-loss kinetic data. In particular, we argue that simplified approaches such as Eq. 4, in which monomer-loss data over the first 10–20% of the aggregation process is utilized, should be considered empirical curve-fitting exercises, from which no underlying mechanistic interpretation of the fitted parameters can be reliably obtained. By truncating the data at early times, as required by the assumptions underlying Eq. 4, one ignores the longer-time data that significantly contributes to differential identification of models (compare Fig. 5 with Fig. 7 *b*). Our analysis calls into question, for example, the conclusion that polyglutamine

peptides, ataxin-3, and β-clam protein aggregation proceed via a thermodynamic nucleus of size $n = 1$ (13–16). Our claim is not that this conclusion is necessarily false. Rather, we claim that no definite conclusion about mechanism is justified based on the published analyses.

An examination of the model equations explains in part why it is difficult to interpret a mechanism, especially based only on monomer-loss data taken at early times. The functional form of the $d[M]/dt$ equations are very similar for many of the different models (for example, compare Eqs. 3, 6, and 7). Greater differences are observed when fibril growth is accounted for. Fibril growth affects kinetic behavior both directly, through the $d[F]/dt$ equations, and indirectly, through the contribution of $[F]$ to the $d[M]/dt$ equations, a contribution that becomes increasingly influential as aggregation progresses. It is important to note that the equations are coupled. For example, the $d[M]/dt$ equations for the PN1 and the SI2 models are identical, but the $d[F]/dt$ equations differ, and since $[F]$ appears in the $d[M]/dt$ equations, the net result is differences in the monomer-loss kinetic patterns. This explains the basis for our result showing that both monomer-loss and fibril-growth data over the entire aggregation process are necessary to discriminate among competing models. It is not possible, using data sets that encompass only the early stages of monomer loss or that lack fibril kinetic data, to adequately distinguish between even simple aggregation models. Indeed, in some of the cases we simulated, insufficient data led to an incorrect conclusion about the underlying mechanism (e.g., Figs. 6 *a*, 7 *a*, and 9 *c*). Robust identification of the underlying kinetic mechanisms requires experimental data on monomer loss that cover the full timespan of the aggregation process, plus measurements of the fibril size (or, equivalently, the fibril molar concentration) over time. Additional experiments to detect the presence of intermediates may be needed to rule out oligomer-based mechanisms, such as the SG model.

Kinetic models and physical interpretation

For the purposes of our study, we derived simple kinetic models that often produced similar, though not identical, modeling equations. Although the model equations may appear mathematically similar, the underlying physics of these models are distinct. The PN model assumes rapid equilibration between monomers and a nucleus with a defined structure. In other words, in the PN model, the nucleus exists as an identifiable species, and the rate of interconversion between the monomer and nucleus is sufficiently fast that the concentration of the nucleus and the monomer are related to each other at all times by the equilibrium constant. A sigmoidal aggregation curve is attributed to a very low equilibrium concentration of nuclei (Fig. 1). In the SI mechanism, irreversible conversion of monomers to an aggregate is assumed, and sigmoidal monomer loss is obtained if the creation of aggregates is slow relative to their growth by monomer addition. In the SI model, the monomer may be conformationally heterogeneous, and there are no defined metastable structured nuclei before the appearance of the smallest fibrils (Fig. 1). A key point of contrast between the PN and the SI models is in the nature of the collision that leads to fibril formation. In the PN1 model, there is a two-step process: first, rapid reversible conversion between the bulk monomer and an alternate conformation (the nucleus), and second, collision between a monomer in the bulk and this rare alternate conformation that produces the first fibril. In the SI2 model, in contrast, a collision between any two monomers in the bulk produces the first fibril. Some of these distinctions between PN- and SI-type schematics are discussed in greater detail in the literature (e.g., (42,43)). In the MP model, one assumes that monomers are initially trapped in two distinct conformations that do not interconvert; as an example, during refolding, a protein may be divided into natively folded and misfolded species, with a large energy barrier separating the two forms. One conformation is then assumed to be capable of initiating aggregation, whereas the other conformation can only add to existing aggregates. The SG model is distinct from the other mechanisms in that oligomeric intermediates are allowed to accumulate until they convert to fibrils. This mechanism posits the appearance of unstructured oligomers that eventually undergo a conformational transition to structured fibrils. Both the MP and SG models require three parameters and both can exhibit sigmoidal aggregation kinetics in multiple mechanistic regimes, especially because the ''monomer'' response is treated as $M_A + M_B$ and $M + nf_n$ in the MP and SG models, respectively.

''Seeding'' is often considered indicative of nucleated growth. We observed, with interest, that the MP model was the most sensitive to seeding of all the mechanisms tested. This result was unexpected, as responsiveness to seeding has sometimes been used as evidence for PN-type mechanisms. We found that the PN and SI models are strongly sensitive to seeding only when the size of the nucleus (n) is large. The response is also strongly dependent on the molar concentration of seeds, a concentration that can be calculated only if one has data on the size of the aggregates used as seeds. Our analysis demonstrates that the mechanism cannot be identified simply by examination of the shape of the monomer-loss kinetic profile or the response to seeding.

In our development of model equations, we focused primarily on monomer-loss mechanisms, because there are more examples in the literature of quantitative analysis of monomer-loss data than of fibril-growth data. Yet, our analysis points out the critical need for experimental data on the size of fibrils and the rate of fibril growth to differentiate among various mechanisms. Monomer addition was the only allowed mechanism for fibril growth in the models we considered. We neglected many of the complexities of fibril growth, such as fibril fragmentation, fibril-fibril coalescence, and formation of off-path agglomerates. Such steps can be readily incorporated into reaction pathways; however,

these steps will involve additional parameters. Thus, accurate parameter estimation and model discrimination for these more complex models will place even greater demands on high-quality fibril data. In particular, these added complexities may necessitate data on the size distribution of fibrils and a more rigorous modeling treatment of distinct F_x species. Nevertheless, the approach developed here can be easily modified to determine whether the data require, for example, that fibril fragmentation or off-path aggregation be considered.

In conclusion, we note that in deriving kinetic model equations from mechanisms, we implicitly assumed that the reaction order is directly related to the reaction stoichiometry. This assumption is almost universally made in the aggregation kinetics field, but it deserves closer examination. This assumption is strictly valid only if the reaction is elementary, that is, if the reaction involves a single reaction step and a single transition state, without any reaction intermediates. Given that a step such as monomer addition to a fibril involves no covalent bond making or breaking, but likely does involve the making and/or breaking of multiple hydrogen bonds, as well as changes in excluded volume and hydrophobic and electrostatic interactions, this assumption may not be justified. If so, the reaction order from fitting kinetic data may be simply empirical and ultimately unrelated to the stoichiometry of the underlying reaction; in other words, a reaction order of 1 does not necessarily imply a stoichiometric coefficient of 1, and vice versa. A simple example suffices to illustrate this difficulty. We consider only monomer addition to preexisting fibrils. If this is an elementary step, then

$$M + F_x \xrightarrow{k_2} F_{x+1}$$

$$\frac{d[M]}{dt} = -k_2[M][F].$$

A plot of the initial rate of monomer loss, $d[M]/dt$, versus $[M]_0$ would be linear, and one would conclude that fibril growth is via monomer addition. However, if monomer addition actually occurs by a two-step mechanism such as the ''dock-lock'' mechanism (44), where F^* represents a fibril where the monomer has docked but not yet locked into place, then the reaction sequence is:

$$M + F_x \underset{k_{-1}}{\overset{k_1}{\rightleftharpoons}} F^*_{x+1}$$

$$F^*_{x+1} \xrightarrow{k_2} F_{x+1}.$$

Assuming that F^* is a reactive intermediate, applying the quasi-steady state assumption, and letting $[F]_{\text{tot}} = \sum[F^*_x] + \sum[F_x]$, we find that $\sum[F^*_x] = k_1[M]\frac{[F]_{\text{tot}}}{k_{-1}+k_2+k_1[M]}$ and the rate of monomer loss is

$$\frac{d[M]}{dt} = -k_1[M][F]_{\text{tot}}\left\{1 - \frac{(k_{-1} - k_1[M])}{(k_{-1} + k_2 + k_1[M])}\right\}.$$

Although the overall reaction is still monomer addition, and the stoichiometry remains the same, the plot of initial rate of monomer loss versus $[M]_0$ is no longer linear. Such effects, if present, further complicate the problem of extracting the aggregation mechanism from kinetic data.

Our results clearly demonstrate the need for more comprehensive kinetic data on protein aggregation, including data that extend over the full timescale of aggregation and comprise multiple measures of aggregate size, structure, and mass. In addition, mechanistic interpretations of kinetic data require clear analysis of the reliability of estimated parameter values and, of more importance, careful statistics-based comparison of several alternative models. The critical importance of distinguishing among various aggregation mechanisms becomes clear as one considers, for example, the possible role of soluble oligomers in cellular toxicity or the design of chemical ligands to prevent aggregation.

SUPPORTING MATERIAL

Seven tables are available at http://www.biophysj.org/biophysj/supplemental/S0006-3495(09)00324-5.

This work was partially supported by a grant (BES-0330537) from the National Science Foundation and a National Research Service Award (T32 GM08293) Molecular Biophysics Predoctoral Training fellowship through the National Institute of General Medical Sciences.

REFERENCES

1. Ross, C. A., and M. A. Poirier. 2005. What is the role of protein aggregation in neurodegeneration? *Nat. Rev. Mol. Cell Biol.* 6:891–898.
2. Cromwell, M. E. M., E. Hilario, and F. Jacobson. 2006. Protein aggregation and bioprocessing. *AAPS J.* 8:E572–E579.
3. Rosenberg, A. S. 2006. Effects of protein aggregates: an immunologic perspective. *AAPS J.* 8:E501–E507.
4. Cottingham, M. G., M. S. Hollinshead, and D. J. T. Vaux. 2002. Amyloid fibril formation by a synthetic peptide from a region of human acetylcholinesterase that is homologous to the Alzheimer's amyloid-β peptide. *Biochemistry.* 41:13539–13547.
5. Goldsbury, C., K. Goldie, J. Pellaud, J. Seelig, P. Frey, et al. 2000. Amyloid fibril formation from full-length and fragments of amylin. *J. Struct. Biol.* 130:352–362.
6. Frieden, C. 2007. Protein aggregation processes: in search of the mechanism. *Protein Sci.* 16:2334–2344.
7. Andrews, J. M., and C. J. Roberts. 2007. A Lumry-Eyring nucleated polymerization model of protein aggregation kinetics: 1. Aggregation with pre-equilibrated unfolding. *J. Phys. Chem. B.* 111:7897–7913.
8. Powers, E. T., and D. L. Powers. 2006. The kinetics of nucleated polymerizations at high concentrations: amyloid fibril formation near and above the ''supercritical concentration''. *Biophys. J.* 91:122–132.
9. Powers, E. T., and D. L. Powers. 2008. Mechanisms of protein fibril formation: nucleated polymerization with competing off-pathway aggregation. *Biophys. J.* 94:379–391.
10. Roberts, C. J. 2007. Non-native protein aggregation kinetics. *Biotechnol. Bioeng.* 98:927–938.

11. Ferrone, F. 1999. Analysis of protein aggregation kinetics. *Methods Enzymol.* 309:256–274.
12. Thakur, A. K., and R. Wetzel. 2002. Mutational analysis of the structural organization of polyglutamine aggregates. *Proc. Natl. Acad. Sci. USA.* 99:17014–17019.
13. Chen, S. M., F. A. Ferrone, and R. Wetzel. 2002. Huntington's disease age-of-onset linked to polyglutamine aggregation nucleation. *Proc. Natl. Acad. Sci. USA.* 99:11884–11889.
14. Bhattacharyya, A. M., A. K. Thakur, and R. Wetzel. 2005. Polyglutamine aggregation nucleation: Thermodynamics of a highly unfavorable protein folding reaction. *Proc. Natl. Acad. Sci. USA.* 102:15400–15405.
15. Ellisdon, A. M., M. C. Pearce, and S. P. Bottomley. 2007. Mechanisms of ataxin-3 misfolding and fibril formation: kinetic analysis of a disease-associated polyglutamine protein. *J. Mol. Biol.* 368:595–605.
16. Ignatova, Z., and L. M. Gierasch. 2005. Aggregation of a slow-folding mutant of a β-clam protein proceeds through a monomeric nucleus. *Biochemistry.* 44:7266–7274.
17. Cellmer, T., R. Douma, A. Huebner, J. Prausnitz, and H. Blanch. 2007. Kinetic studies of protein L aggregation and disaggregation. *Biophys. Chem.* 125:350–359.
18. Krzewska, J., M. Tanaka, S. G. Burston, and R. Melki. 2007. Biochemical and functional analysis of the assembly of full-length Sup35p and its prion-forming domain. *J. Biol. Chem.* 282:1679–1686.
19. Morris, A. M., M. A. Watzky, J. N. Agar, and R. G. Finke. 2008. Fitting neurological protein aggregation kinetic data via a 2-step, Minimal ''Ockham's Razor'' model: the Finke-Watzky mechanism of nucleation followed by autocatalytic surface growth. *Biochemistry.* 47:2413–2427.
20. Gibson, T. J., and R. M. Murphy. 2006. Inhibition of insulin fibrillogenesis with targeted peptides. *Protein Sci.* 15:1133–1141.
21. Chen, Y. D., K. Bjornson, S. D. Redick, and H. P. Erickson. 2005. A rapid fluorescence assay for FtsZ assembly indicates cooperative assembly with a dimer nucleus. *Biophys. J.* 88:505–514.
22. Collins, S. R., A. Douglass, R. D. Vale, and J. S. Weissman. 2004. Mechanism of prion propagation: amyloid growth occurs by monomer addition. *PLoS Biol.* 2:1582–1590.
23. Ruschak, A. M., and A. D. Miranker. 2007. Fiber-dependent amyloid formation as catalysis of an existing reaction pathway. *Proc. Natl. Acad. Sci. USA.* 104:12341–12346.
24. Dubay, K. F., A. P. Pawar, F. Chiti, J. Zurdo, C. M. Dobson, et al. 2004. Prediction of the absolute aggregation rates of amyloidogenic polypeptide chains. *J. Mol. Biol.* 341:1317–1326.
25. Chiti, F., M. Calamai, N. Taddei, M. Stefani, G. Ramponi, et al. 2002. Studies of the aggregation of mutant proteins in vitro provide insights into the genetics of amyloid diseases. *Proc. Natl. Acad. Sci. USA.* 99:16419–16426.
26. Chiti, F., N. Taddei, F. Baroni, C. Capanni, M. Stefani, et al. 2002. Kinetic partitioning of protein folding and aggregation. *Nat. Struct. Biol.* 9:137–143.
27. Ellisdon, A. M., B. Thomas, and S. P. Bottomley. 2006. The two-stage pathway of ataxin-3 fibrillogenesis involves a polyglutamine-independent step. *J. Biol. Chem.* 281:16888–16896.
28. Colby, D. W., J. P. Cassady, G. C. Lin, V. M. Ingram, and K. D. Wittrup. 2006. Stochastic kinetics of intracellular huntingtin aggregate formation. *Nat. Chem. Biol.* 2:319–323.
29. Nielsen, L., R. Khurana, A. Coats, S. Frokjaer, J. Brange, et al. 2001. Effect of environmental factors on the kinetics of insulin fibril formation: elucidation of the molecular mechanism. *Biochemistry.* 40:6036–6046.
30. Chirita, C. N., E. E. Congdon, H. S. Yin, and J. Kuret. 2005. Triggers of full-length τ aggregation: a role for partially folded intermediates. *Biochemistry.* 44:5862–5872.
31. Pedersen, J. S., D. Dikov, and D. E. Otzen. 2006. N- and C-terminal hydrophobic patches are involved in fibrillation of glucagon. *Biochemistry.* 45:14503–14512.
32. Koo, B. W., J. A. Hebda, and A. D. Miranker. 2008. Amide inequivalence in the fibrillar assembly of islet amyloid polypeptide. *Protein Eng. Des. Sel.* 21:147–154.
33. Caracotsios, M., and W. E. Stewart. 1985. Sensitivity analysis of initial-value problems with mixed ODEs and algebraic equations. *Comput. Chem. Eng.* 9:359–365.
34. Caracotsios, M., and W. E. Stewart. 2008. Computer-Aided Modeling of Reactive Systems. Wiley. Hoboken, NJ.
35. Stewart, W. E., M. Caracotsios, and J. P. Sorensen. 1992. Parameter estimation from multiresponse data. *AIChE J.* 38:641–650.
36. Stewart, W. E., Y. Shon, and G. E. P. Box. 1998. Discrimination and goodness of fit of multiresponse mechanistic models. *AIChE J.* 44:1404–1412.
37. Lee, C. C., R. H. Walters, and R. M. Murphy. 2007. Reconsidering the mechanism of polyglutamine peptide aggregation. *Biochemistry.* 46:12810–12820.
38. Xue, W.-F., S. W. Homans, and S. E. Radford. 2008. Systematic analysis of nucleation-dependent polymerization reveals new insights into the mechanism of amyloid self-assembly. *Proc. Natl. Acad. Sci. USA.* 105:8926–8931.
39. Hammarstrom, P., X. Jiang, A. R. Hurshman, E. T. Powers, and J. W. Kelly. 2002. Sequence-dependent denaturation energetics: a major determinant in amyloid disease diversity. *Proc. Natl. Acad. Sci. USA.* 99:16427–16432.
40. Kayed, R., J. Bernhagen, N. Greenfield, K. Sweimeh, H. Brunner, et al. 1999. Conformational transitions of islet amyloid polypeptide (IAPP) in amyloid formation in vitro. *J. Mol. Biol.* 287:781–796.
41. Khare, S. D., F. Ding, K. N. Gwanmesia, and N. V. Dokholyan. 2005. Molecular origin of polyglutamine aggregation in neurodegenerative diseases. *PLOS Comput. Biol.* 1:230–235.
42. Pappu, R. V., X. Wang, A. Vitalis, and S. L. Crick. 2008. A polymer physics perspective on driving forces and mechanisms for protein aggregation. *Arch. Biochem. Biophys.* 469:132–141.
43. Vitalis, A., X. Wang, and R. V. Pappu. 2008. Atomistic simulations of the effects of polyglutamine chain length and solvent quality on conformational equilibria and spontaneous homodimerization. *J. Mol. Biol.* n press.
44. Esler, W. P., E. R. Stimson, J. M. Jennings, H. V. Vinters, J. R. Ghilardi, et al. 2000. Alzheimer's disease amyloid propagation by a template-dependent dock-lock mechanism. *Biochemistry.* 39:6288–6295.